

Research Article

Study of Simulation Test in Inclusion Rockburst

Zhidong Wang ^{1,2,3}, Liyun Li ^{1,2}, Bingquan Liu,² Chuang Han,² and Tianxiang Lan²

¹State Key Laboratory of Coal Resources and Safe Mining, China University of Mining and Technology (Beijing), Beijing 100083, China

²School of Mechanics and Civil Engineering, China University of Mining and Technology (Beijing), Beijing 100083, China

³Guodian United Power Technology Company Limited, Beijing 100039, China

Correspondence should be addressed to Zhidong Wang; wangzhidong1116@126.com and Liyun Li; lly@cumtb.edu.cn

Received 12 October 2018; Accepted 25 December 2018; Published 27 January 2019

Academic Editor: Raffaele Landolfo

Copyright © 2019 Zhidong Wang et al. This is an open access article distributed under the Creative Commons Attribution License, which permits unrestricted use, distribution, and reproduction in any medium, provided the original work is properly cited.

Based on the existing classification research of rockburst dynamic disasters, a new rockburst model is introduced. The model specimens with inclusion rock are designed and produced, and the indoor test of inclusion rockburst with or without cementation, different inclusion angles, and prefabricated cracks of different lengths is carried out. The failure process and displacement variation of rock specimens are recorded and measured by the high-speed camera system and digital image correlation method, and based on this, the characteristics and laws of rockburst are analyzed. The results show that the failure process of inclusion rock can be divided into several periods, such as crushing and extrusion of the cement body, and the cracks in the upper left tip, the lower right tip, the lower left tip, and the upper tip are expanded and broken in different orders. The dynamic ejection failure of the rock fragments occurs when the degree of failure is severe, and the static failure occurs when the degree of failure is weak. The inclusions have cementation, and the better the cementation, the greater the stress loading required in the failure, the greater the energy accumulated, the more severe the failure, and the higher the fractal dimension of the fragments. The larger the angle of the inclusion tip, the greater the stress loading in failure; the greater the change of the u and v displacements, the more the displacement of the inclusions changed; and the more the energy accumulated, the higher the fractal dimension of the fragment. The smaller the crack length, the greater the stress loading in failure, and the more the energy accumulated, the higher the fractal dimension of the fragments in failure. With more number of cracks and the more severe expansion before failure, the failure of rock mass can be transformed from the dynamic to the static.

1. Introduction

Rockburst is a common rock dynamic failure phenomenon in underground engineering and mining engineering [1–3], which is featured by huge sound, air waves, and spontaneous rock stripping and quick rock ejection, bringing casualties, damage of construction equipment, and underground engineering scrap. Therefore, the rockburst belongs to a dynamically static geological disaster. The classification of dynamic disasters on rockburst is one of the most fundamental and key scientific issues on rockburst research. Many experts have classified rockburst from the mechanism, location, and failure manifestation. Based on five international authoritative scholars on the mechanism and definition of rockburst, Qian and Zhou [4] proposed that the rockburst

should be divided into fault slip or fault slip and rock strain types caused by rock failure. Based on the energy accumulation and transformation characteristics of rockburst, He et al. [5] proposed that rockburst should be divided into the types of single energy induced and composite energy conversion induced, and the single energy type can be divided into the type of solid energy induced, gas energy induced, liquid energy induced, roof falling energy induced, and tectonic energy induced. Based on the caused sudden instability, failure of coal and rock mass from the stress state, the common geological structure, and mining process characteristics, Jiang et al. [6] proposed the rockburst of coal mine can be divided into material instability, slip displacement, and structural instability. Xu and Wang [7] divided rockburst into self-heavy stress, tectonic stress,

variable stress, and comprehensive stress from the cause of high ground stress on rock mass of rockburst.

In order to study the mechanism of rockburst, the relevant experts have carried out a large number of laboratory experiments on the basis of the existing rockburst classification and have obtained many valuable research results. Xie et al. [8] pointed out that the energy release of rock structure after energy dissipation was studied from the perspective of the macroscopic energy conservation, which can be used to estimate the intensity of damage in the project or the ejection velocity of the fractured rock and quantitatively analyze the energy transfer process in the rock structure. Li et al. [9] carried out a spallation failure test on granite specimens by the semisinusoidal waveform generated with the modified Hopkinson pressure bar device, and the crack failure process of the specimens is recorded by the high-speed camera. Zhou et al. [10] carried out the buckling rockburst simulation test by a similar rock material and analyzed the failure process and characteristics of the plate buckling rock. Dyskin and Germanovich [11] analyzed the formation causes of slab-type rockburst, it is believed that the stress concentration of surrounding rock caused by excavation promotes the stable expansion of primary fractures, the vacant surface causes the crack to expand unsteadily along the direction parallel to the rock wall, and the rock plate fracture and the surrounding rock are suddenly separated and ejected out. Li et al. [12] carried out a similar material test to simulate the rockburst caused by tunnel excavation, indicating that the tunnel in the field is dominated by spalling and drum-type tensile failure. Gong et al. [13] carried out a three-dimensional loading test on specimens with prefabricated holes by a true triaxial rock test system and reproduced the whole process of plate buckling rockburst in a deep buried hard rock circular tunnel. Su et al. [14] carried out the physical test of the strained rockburst on the cuboid granite by the true triaxial test system and analyzed the characteristics and laws of the failure process on rockburst. Zuo et al. [15] studied the velocity of the failure block in the buckling rockburst under static loading and dynamic-static combined loading from the perspective of energy balance. Zuo et al. [16] studied the deformation and failure characteristics of different coal-rock combinations and the association with dynamic disasters. Sun et al. [17] analyzed the temperature field and displacement field evolution law and model instability failure mechanism during the test of a weak broken surrounding rock tunnel by the noncontact monitoring method.

The above research results have greatly enriched the existing occurrence mechanism of various types of rockburst and have important significance for the prevention and control of rockburst. However, the mechanism of rockburst is extremely complicated, and there is no unified and clear theoretical explanation for rockburst. Therefore, based on the engineering site and other existing inclusion materials research [18, 19], the model of inclusion rockburst is proposed, and the model specimen with inclusions is designed and processed. The indoor physical test on ejection process of inclusion rockburst is carried out by the high-speed camera and digital image correlation method (DIC), which realizes the real-time monitoring and recording of the

whole process of the test, reproduces the rockburst process of the inclusion rockburst, and the test process and results are analyzed in detail so as to study the mechanism of the inclusion rockburst.

2. Inclusion Rockburst

The author found that the rock fragments on the roadway surface were exfoliated and ejected out in the ventilation roadway of the working face 0092 of Jinggezhuang mine of Kailuan Group, and the rock fragments that were peeled off and ejected to the ground were not the same rock type (siltstone and maroon mudstone), the failure craters and nearby areas formed on the roadway surface are also divided into two color regions, a small part of areas is brownish red (mudstone) and other rocky areas is gray (siltstone), and a small part of the area and the boundary part are more seriously damaged. Based on the geological data of the mine and related literature, the rock mass structure is an inclusion or inclusion layer, and the research on failure of inclusion rock in mining and rock engineering is lesser; however, a few experts have carried out some research on the inclusion problems of other materials. Therefore, the inclusion rockburst model is proposed on the study of rockburst in this paper. In other words, the inhomogeneity of stratigraphic sedimentation and complex geological effects result in the nonuniform monolithic rock mass in the complex rock mass structure. Different rock geological bodies are cemented together by cement and compressed by the sedimentary layer to form inclusions, which are characterized by small volume of geological bodies being wrapped by larger volume of geological bodies, and it shows a small volume of geological bodies is wrapped by a larger volume of geological bodies. When the excavation of rock mass is close to the inclusion rock mass, the stress concentration near the rock and coal surface appears. When the rock nearby inclusions continue to be excavated, the pressure is more concentrated under the shear stress, and a part of inclusions and the cement are crushed, which lose the cementation effect so that the inclusions are crushed and sheared and ejected out, resulting in the occurrence of rockburst (Figure 1).

Therefore, the inclusion model specimens are designed and processed, considering the angles of the inclusions and prefabricated cracks in rock specimens. The model test is used to simulate the occurrence process and phenomena of inclusion rockburst in rock mass engineering, the digital image correlation method is used to study the deformation field of the surface of inclusion rock, and the high-speed camera is used to obtain the failure law of the surface of the specimens and the fragments in the ejection, which explores the mechanism of inclusion rockburst, triaxial rock test system of State Key Laboratory of Coal Resources and Safe Mining (Figure 2).

3. Simulation Test of Inclusion Rockburst

3.1. Parameters Test of the Rock. The rock sample is derived from the shale with good uniformity and complete integrity in the diversion tunnel of Longtan Hydropower Station. The rock material is processed into six standard cylindrical

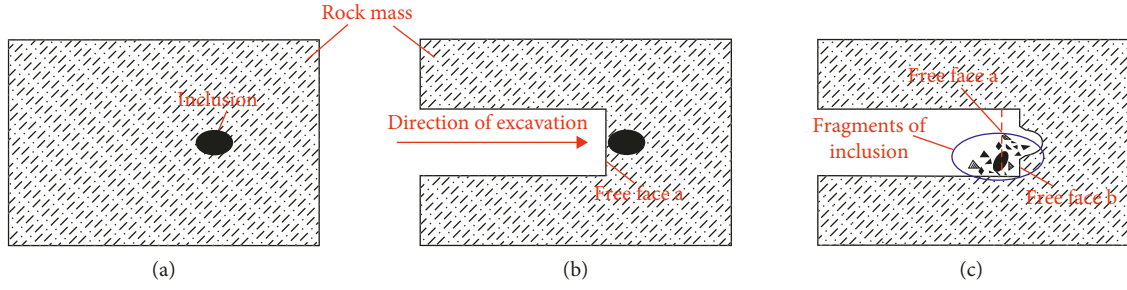


FIGURE 1: Inclusion rockburst. (a) Unexcavated; (b) excavated near the inclusions; (c) the failure in further excavation of inclusions.

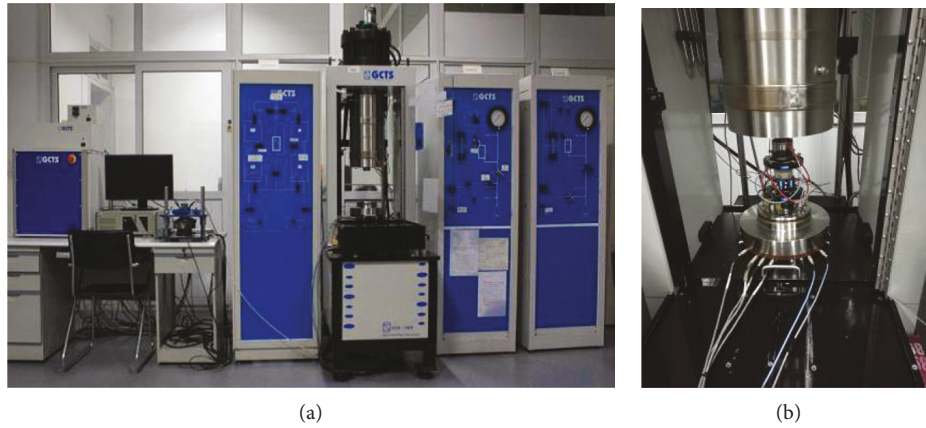


FIGURE 2: GCTS triaxial rock testing. (a) GCTS triaxial rock testing system. (b) Testing layout.

specimens of $\varnothing 50 \text{ mm} \times 100 \text{ mm}$. The triaxial rock test system (GCTS) is used to carry out the uniaxial compression experiment on the specimens through displacement loading; the maximum tonnage of the testing machine is 100 t, and the loading speed is 0.05 mm/min. The mechanical parameters of the rock material can be obtained in the stress-strain curves of specimens, and the conventional calculation formulas, such as incremental method, and all of which are shown in Table 1.

Based on the entire stress-strain curve and the loading and unloading curves of the conventional specimens of shale measured by the triaxial testing machine, the relevant parameters obtained by the calculation formula can be used to judge the rockburst proneness of the shale, including elastic deformation energy index W_{ET} , burst energy index K_{cf} , brittleness index B , and maximum elastic strain energy E_s [20–23].

3.1.1. Elastic Deformation Energy Index W_{et} . When the shale specimen is subjected to 80% of the peak strength in the uniaxial compression test, the stress-strain curve can be obtained. Thus, the elastic deformation energy E_e and the plastic deformation energy E_p are obtained, and elastic deformation energy index W_{et} can be obtained from the following formula:

$$W_{et} = \frac{E_e}{E_p}. \quad (1)$$

Criteria for rockburst proneness: $W_{et} : W_{et} \geq 5.0$, strong rockburst proneness; $3.5 \leq W_{et} < 5.0$, medium rockburst proneness; $2.0 \leq W_{et} < 3.5$, weak rockburst proneness; and $W_{et} < 2.0$, no rockburst proneness.

3.1.2. Burst Energy Index K_{cf} . Based on the whole process curve of stress and strain of shale, the area F_1 surrounded by the curve and the strain axis before the stress peak and the area F_2 surrounded by the curve and the strain axis after the stress peak are, respectively, calculated, and the burst energy index K_{cf} can be obtained from the following formula:

$$K_{cf} = \frac{F_1}{F_2}. \quad (2)$$

Criteria for rockburst proneness: $W_{et} : K_{cf} \geq 3.0$, strong rockburst proneness; $2.0 \leq K_{cf} < 3.0$, medium rockburst proneness; $1.0 \leq K_{cf} < 2.0$, weak rockburst proneness; and $K_{cf} < 1.0$, no rockburst proneness.

3.1.3. Brittleness Index B . The brittleness index B is the ratio of the uniaxial compressive strength σ_c to the tensile strength σ_t , which reflects the brittleness degree of the rock. The larger the brittleness index, the more likely the rockburst occurs:

$$B = \frac{\sigma_c}{\sigma_t}. \quad (3)$$

TABLE 1: Mechanical parameters of shale and rockburst proneness.

Density (g·cm ⁻³)	Compressive strength (MPa)	Tensile Strength (MPa)	Elasticity modulus (GPa)	Poisson's ratio	Elastic deformation energy index, W_{ET}	Burst energy index, K_{cf}	Brittleness index, B	Maximum elastic strain energy (MJ/m ³)
2.7	80	0.8	10	0.26	3.6 medium rockburst	2.3 medium rockburst	16.7 medium rockburst	0.35 weak rockburst

Criteria for rockburst proneness are given as follows: B : $B \geq 40$, no rockburst proneness; $26.7 \leq B < 40$, weak rockburst proneness; $14.5 \leq B < 26.7$, medium rockburst proneness; and $B < 14.5$, strong rockburst proneness.

3.1.4. *Maximum Elastic Strain Energy E_s* . The maximum elastic strain energy E_s stored in the standard specimen of shale is as shown in the following formula, where E is the elastic modulus of the rock:

$$E_s = \frac{\sigma_c^2}{2E} \quad (4)$$

Criteria for rockburst proneness are given as follows: E_s : $E_s < 0.20$ MJ/m³, no rockburst proneness; $0.2 \leq E_s < 0.5$ MJ/m³, weak rockburst proneness; $0.5 \leq E_s < 0.75$ MJ/m³, medium rockburst proneness; and $E_s \geq 0.75$ MJ/m³, strong rockburst proneness.

Therefore, based on the four rockburst proneness indicators and the discriminant criteria obtained from the above calculations, the preliminary rockburst proneness of shale is shown in Table 1.

3.2. Test of Inclusion Rockburst

3.2.1. *Preparation of Rock Samples*. The shale sample is processed into the cuboid specimen with an overall size of 76 mm × 50 mm × 30 mm. The symmetrical triangular cylinder is cut in the middle of every rock specimen. Since the inclusion rockburst model is proposed for the first time, the tests are carried out twice. The first batch is a tentative simulation test, and the second test is based on the first test to optimize the test. Therefore, in the first test, the angle of the tip of the triangular cylinder (inclusion body) of the rock specimen is 20° and the tip side is 12 mm from the left and right side. The same has been proceeded in two specimens, which are, respectively, labeled as specimen 1# and specimen 2# (Figure 3(a)). The second batch of specimens is processed with four shale specimens, namely, 3#, 4#, 5#, and 6#. Four specimens are prefabricated symmetric cracks; the outer crack tip is 11 mm from the bottom, and the angle between the crack and the horizontal is 30°. In order to study the effect of crack length a on the failure of the specimen, the crack length of specimen 3# and specimen 6# is 6.5 mm, and the crack length of specimen 4# and specimen 5# is 5.5 mm. Similarly, in order to analyze the effect of the inclusion angle θ on the failure, the tip angle θ of specimens 3# and 4# is 40°, and the tip angle θ of specimens 5# and 6# is 30°, which is shown in Figure 3(b)

In order to understand the effect of cement on the inclusion rockburst, the two triangular cylinders (inclusions) are put directly in the triangle areas of specimen 1# without cementation (Figure 4). The two triangular cylinders (inclusions) are cemented in the cut triangle area of specimens 2#, 3#, 4#, 5#, and 6#, which are cured for one week (Figure 3(c)). The cement material is Anda 42.5 grade fast hard sulphoaluminate cement, and the compressive strength of cement is 53.3 MPa, the modulus of elasticity is 0.22 GPa, Poisson's ratio is 0.16, and the water-cement ratio is 0.6 [24]. The physical and mechanical parameters of the shale are shown in Table 1.

3.2.2. *The Layout of Test System*. The uniaxial compression test of specimens 1#, 2#, 3#, 4#, 5#, 6# is carried out by the GCTS triaxial rock test system. Since the diameter ϕ of the indenter and base of the system is 50 mm, two discs of the same stiffness are placed between the specimen and the indenter and base of the test machine, the diameter ϕ of the disc is 100 mm, and the stiffness of the disc is 1.75 mN/mm. The rate of displacement loading is 0.05 mm/min. Since the first test is a tentative test, the video recording of the specimens 1# and 2# is performed only by a normal camera. The uniaxial compression test of specimens 3#, 4#, 5#, and 6# is carried out at the same displacement loading rate in the second test; the high-speed camera FASTCAM1.1 and the digital camera MV-VD500SM/SC are used to synchronously record the deformation process of the specimen in the loading process. The photo interval of the high-speed camera is 0.001333 s, and the time interval of the digital camera is 1 s. The test system is shown in Figure 5.

3.3. *The Result of Rockburst Test*. Due to the relatively high rigidity of the disc pad, the pad hardly affects the result of specimens in this test. Therefore, Figure 4 shows the whole process stress-strain curve of specimens 1#, 2#, 3#, 4#, 5#, and 6#. Ejection failure occurred in specimens 1#, 2#, 4#, 5#, and 6#, and static brittle failure occurred in specimen 3#. The prepeak curves of the specimens 1#, 2#, 3#, 4#, and 5# have obvious compaction stages, and specimen 6# directly skips the compaction stage on account of the test operation factors in the typical stress-strain curve. The fluctuations of curve in the prepeak stress correspond to the failure phenomenon in the test, respectively. The crack initiation, expansion failure, ejection of the penetration region and inclusions, shear failure of the specimen as a whole from the tip of the inclusion body, and sounds of different sizes are accompanied. After reaching the peak stress, the curve drops sharply, and

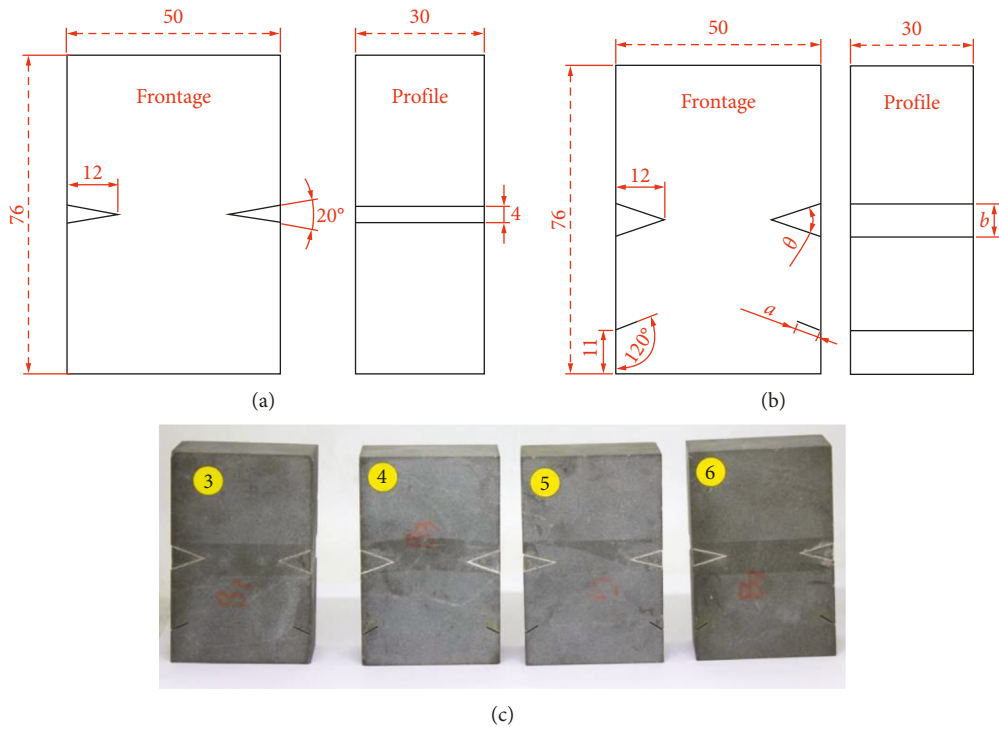


FIGURE 3: Inclusion rock specimens. (a) The size of specimens 1# and 2#. (b) The size of specimens 3#, 4#, 5#, and 6#. (c) Specimen appearance.

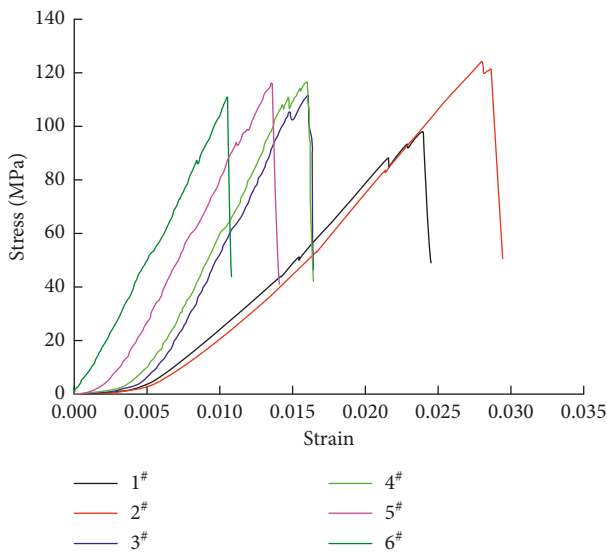


FIGURE 4: Axial stress-strain curves of model specimens.

the curve is steep, which is fully manifested as brittle failure of the specimen.

In order to describe in detail the occurrence process of the inclusion rockburst test, it is analyzed and shown as Figure 4 and Table 2.

3.3.1. Test of Specimen 1#. Since the test of specimen 1# is tentative, it is only recorded by a normal camera, and the resolution and time interval of the captured image are low,

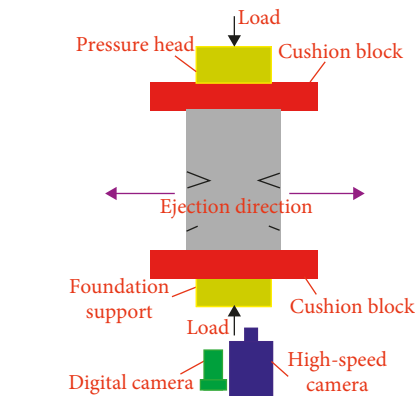


FIGURE 5: The layout of rockburst test system.

and the typical failure process is as shown in Figure 6. The color of the tip gradually becomes white with the increase of the load, which indicates that the part is concentrated in stress and the damage of the tip is obvious. When the axial stress σ_z is 88.39 MPa, the stress-strain curve shows a drop fluctuation. The tip of the right inclusion of the specimen is cracked at this time, and the reverse crack with a crack angle of 95° is extended downward to the bottom of the specimen. The cracked rock mass and the right inclusion are rapidly ejected (Figure 6(b)), accompanying with a crisp sound. The white part of the left and right inclusions became more and more obvious during the loading process, and the new defects gradually became produced. When the stress σ_z is 93.42 MPa, the curve showed small fluctuations, and the right tip showed an airfoil crack with a crack angle of 70°

TABLE 2: Test results of inclusion rockburst

Specimen number	Peak load P (kN)	Axial displacement (mm)	Axial stress (MPa)	Axial strain	Failure characteristics
1#	147.336	1.814	98.224	0.02387	Two blocks ejection at the lower right side + shear failure
2#	186.692	2.130	124.462	0.02802	Two crack initiation + left inclusion ejection + shear failure
3#	168.351	1.221	112.234	0.01601	Six crack cracking + cement ejection + particle, flake ejection
4#	174.901	1.211	116.627	0.01593	Ejection of rock and inclusion on left front and rear right
5#	174.206	1.030	116.137	0.013355	Ejection of left inclusion and left upper and lower rock + shear failure
6#	166.611	0.8	111.074	0.010526	Ejection of left and right inclusion

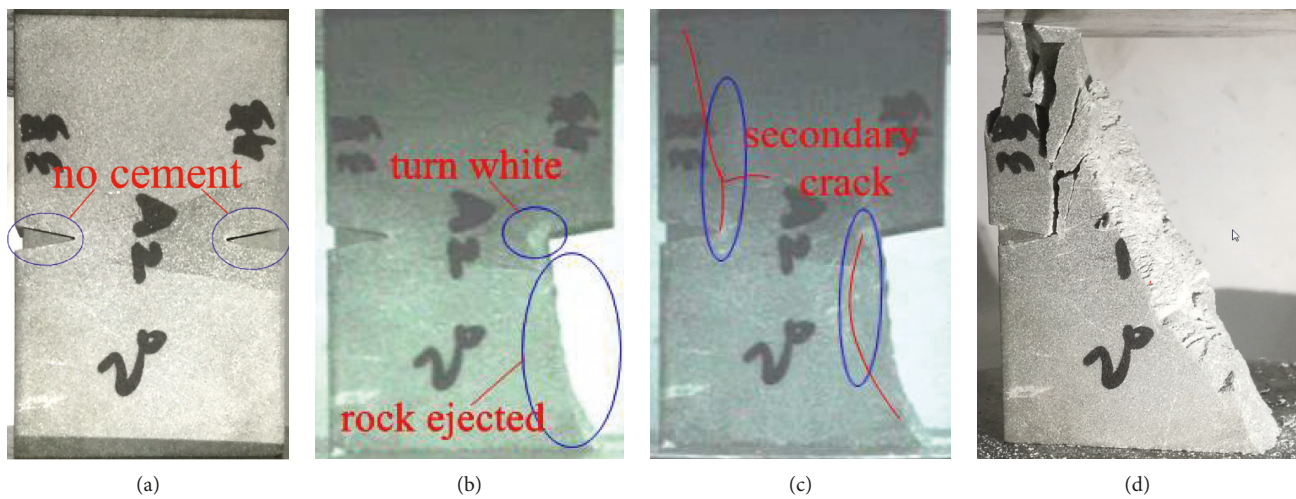


FIGURE 6: The failure process of specimen 1#. (a) Original state. (b) First ejection (88.39 MPa). (c) Second ejection (93.42 MPa). (d) After failure.

(Figure 6(c)). The stress loading continues to last for 6 seconds. When the peak stress σ_z of 98.22 MPa is reached, the airfoil crack gradually expands to the bottom of the specimen, and the rock mass formed by the airfoil crack and the reverse crack is ejected again, accompanying with a loud sound. The left tip is cracked in the angle of 90° at the same time, and when it is extended upward by 11.57 mm, the vertical bifurcation appears to the right and extends to the top of the specimen and the main shear fracture zone, respectively. Finally, the overall shear failure of the specimen occurs, which is shown in Figure 6(d). Two large rockbursts occurred on the right side of specimen, and small particles and flaky projectiles occurred locally during the entire failure process.

3.3.2. Test of Specimen 2#. The test of specimen 2# is also tentative. Based on the concentrated force and obvious damage, the color gradually becomes white during the loading process. When the axial stress σ_z is 83.88 MPa, the tip of the right inclusion is cracked, and the white reverse crack 1# with a crack angle of 85° is expanded downward (Figure 7(a)). The white part of the left and right inclusions

became more and more obvious during the loading process. When the peak stress σ_z is 124.46 MPa, a second airfoil crack 2# with a cracking angle of 70° appears on the right tip, and the airfoil crack 3# with a cracking angle of 80° appears on the left tip (Figure 7(b)). The internal damage zone results in a decrease in the overall load carrying capacity of the specimen; however, the overall failure appears on the specimen. The curve continues to rise from the peak stress 119.76 MPa. The stress σ_z is 121.49 MPa after 28 seconds of continuous loading; crack 4# with the crack angle of 65° appears on the left tip (Figure 7(c)), and it gradually expands to the top of the specimen. The video shows that the left inclusion is ejected out, the connect of cracks 1# and 4# makes the upper left part of the specimen eject out, and the connect of cracks 2# and 3# makes the lower right rock and the right inclusion eject out (Figure 7(d)). Finally, the specimen is subjected to overall shear failure based on the shear band.

It can be found that the process of inclusion rockburst can be summarized that the stress concentration of the tip part of the inclusion body results in serious damage, secondary cracks appearing and expanding up and down; inclusions and the nearby cracked rock mass are ejected out

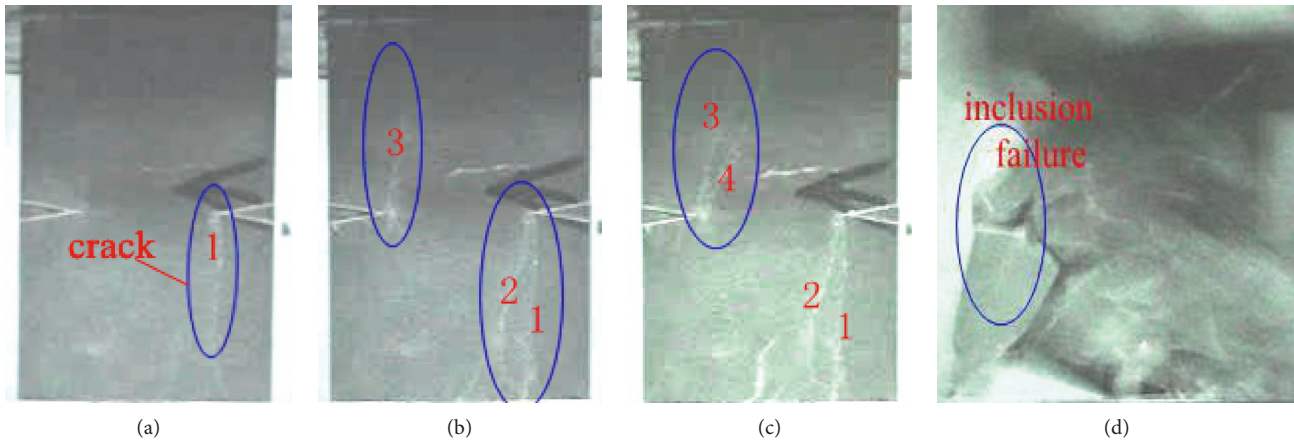


FIGURE 7: The failure process of specimen 2#. (a) The appearance of crack 1# (83.88 MPa). (b) The appearance of cracks 1# and 2# (124.46 MPa). (c) The appearance of crack 4# (121.49 MPa). (d) The ejection of inclusion.

from the tentative test of specimens 1# and 2#. The inclusions are cemented with the surrounding rock mass for a long time in the rock mass engineering, so the cemented specimen 2# is more common in the study of rockburst. Based on the cementation of the cement in specimen 2#, a large load required in failure may cause hidden dangers to the safety of equipment and human in the laboratory. Simultaneously, in order to study the influence of rock defects on the inclusion rockburst, symmetrical cracks are prefabricated near the bottoms of specimens 3#, 4#, 5#, and 6# in left and right side by high-speed cameras and digital cameras.

3.3.3. Test of Specimen 3#. When the axial stress σ_z is 102.79 MPa in the loading of the specimen 3#, secondary cracks 1# and 2# appear at the tip of the lower left prefabricated crack, and the reverse crack 1# with a cracking angle of 123° extends straightway from the tip to the bottom of the specimen; the airfoil crack 2# with a cracking angle of 20° gradually extends from the tip end downward to the bottom of the specimen at an arc angle (Figure 8(a)). When the axial stress σ_z is 106.01 MPa, crack 3# and crack 4# appear at the tip of the left inclusion, and crack 3# appears from the tip of the inclusion at an angle of 103° and continues to expand downward at different angles, which connects to crack 2#. The connecting crack at the bottom of the specimen is 4.52 mm from the left bottom end point. Crack 4# with the cracking angle of 30° connects to the end of lower left crack (Figure 8(b)). When $\sigma_z = 111.27$ MPa, the curve shows a drop state with sound, and the crack at the left tip has a crack angle of 20° , which gradually expands to the bottom of the test piece with a curved line, and the distance from the end of the crack to the end of the left bottom is 14 mm (Figure 8(c)).

When the axial stress σ_z is 111.27 MPa, the curve shows a drop state with sound, and the crack 5# at the left tip with a cracking angle of 20° gradually expands to the bottom of the specimen with an arc line, and the distance from the end of the crack to the end of the left bottom is 14 mm (Figure 8(c)). The peak stress σ_z is 112.23 MPa at loading, the failure of specimen is accompanied by a large violent sound, and the

cement between the left and right inclusions and the surrounding rock is crushed (white). Based on cracks 3#, 4#, and 5#, an arc-shaped crack 6# appears. The end of the cut-through crack at the bottom is 19.24 mm from the end point of the left bottom of the specimen. The cut-through area of the left inclusion body and cracks 3#, 4#, 5#, and 6# only appears as static failure and is not ejected out; the reason is that more cracks in this part appear, the accumulated strain energy is mostly consumed by the surface energy during the fracture process, and the remaining energy is not enough to be converted into the projectile kinetic energy. Vertical upward crack 7# and crack 8# sheared in the specimen appear in the right end of the inclusion body, crack 8# combines with crack 6# and 7#, and the surface energy of the fracture of the right part of the specimen also greatly consumes the strain energy accumulated during the loading process, resulting in specimen 3# only undergoing static brittle failure without rockburst (Figure 8(d)).

Since the energy accumulated in specimen 3# is consumed by the surface energy of more cracks, no violent rock eruption occurs, and it is only accompanied by the ejection of a small number of small rock particles on the surface and the cement between the inclusions and the specimen in initiation and cracking of the crack (Figure 9). In order to assess the threat to the surrounding rock during rockburst, the extent of the failure is characterized by the ejection velocity of the rock fragments.

The continuous photos taken by the high-speed camera are imported into MATLAB to obtain the displacement of the rock fragments ejected in different photos. The time difference between the photos is known, so the moving displacement of the fragments is divided by the time difference to calculate the ejection velocity of the fragments. The ejection velocities of the fragments during the ejection has been constantly changing and decreasing, so the extent of the ejection failure is characterized by calculating the initial velocities. Since there are no ejection failures of the rock fragments and only the ejection of the cement fragments in specimen 3#. Therefore, based of Figures 9(a) and 9(b) in MATLAB, the displacement of the upper right cement in 0.001333 seconds is (5.0622 mm, 1.2273 mm) in

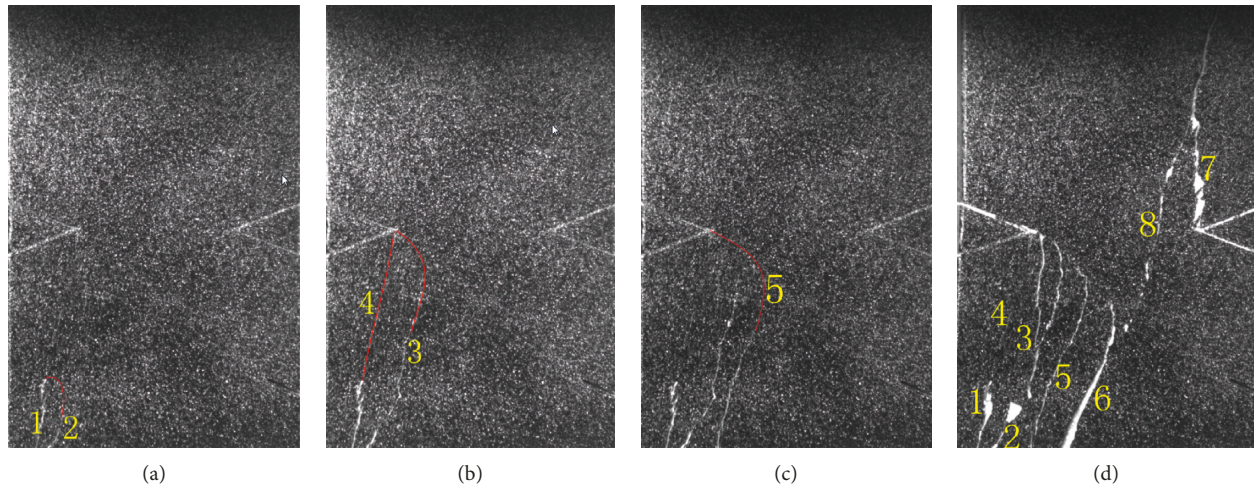


FIGURE 8: The failure process of specimen 3#. (a) $\sigma_z = 102.79$ MPa. (b) $\sigma_z = 106.01$ MPa. (c) $\sigma_z = 111.27$ MPa. (d) $\sigma_z = 112.23$ MPa.

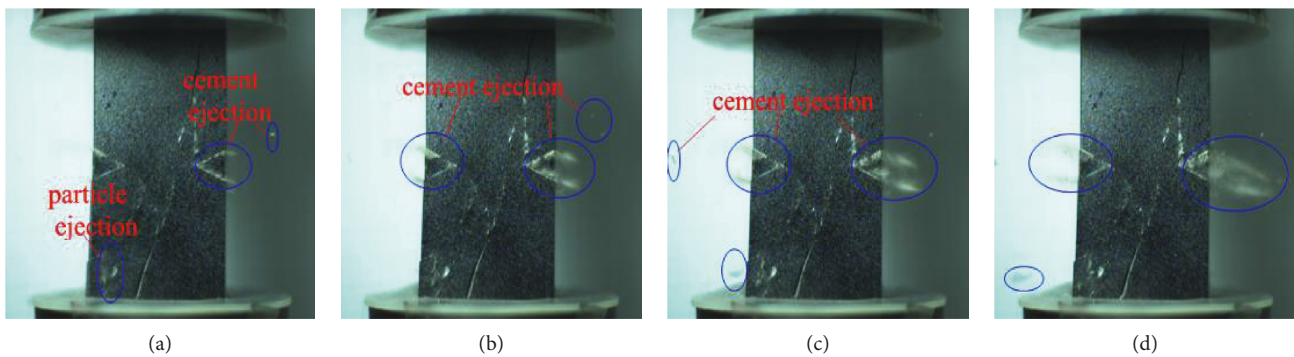


FIGURE 9: The ejection failure of specimen 3#. (a) 0.484000 s. (b) 0.482667 s. (c) 0.481333 s. (d) 0.480000 s.

horizontal and vertical coordinates; similarly, the displacement of the lower right cement is (5.96826 mm, 0.4602), the displacement of upper left cement is (1.0738 mm, 0.3615 mm) and the displacement of lower left cement is (1.8408 mm, 0.3068 mm). The ejection velocity is 3.9076 m/s on the upper right, 4.5014 m/s on the lower right, 0.8450 m/s on the upper left, and 1.4000 m/s on the lower left.

3.3.4. Test of Specimen 4#. When the axial stress σ_z is 108.25 MPa in the loading of the specimen 4#; it suddenly falls to 107.67 MPa, and the end of left lower preformed crack of specimen 4# is cracked upward at a crack angle of 49° . When the axial stress σ_z reaches 110.98 MPa in the continued loading, the curve shows a large drop, and the reverse crack at the tip of the left inclusion has a crack angle of 103° , while the lower left prefabricated crack continues to expand upward, and two secondary cracks grow and break (Figure 10(a)), and an instantaneous unloading phenomenon appears, accompanying with sound. The curve continues to rise after it drops to 106.64 MPa. When the peak stress σ_z is 116.627 MPa, the left front prefabricated crack combines with the secondary crack generated by the tip of the inclusion, and the part of the rock together with the

inclusion is broken and ejected out (Figure 10), accompanied by a crisp sound. The shear failure appears on specimen 4# and grows to the end of left preformed crack. The left front inclusion is cemented together with the rock in the initial stage of the ejection, the two gradually split, and some white and damaged fragments of the internal part are successively ejected out from the failure area during the ejection process. At the same time, similar failure occurs in the right rear of the specimen; the difference is that the right rear inclusion and the broken rock are separated and ejected out at the initial stage of the rockburst. The crack generated at the tip of the right inclusion is expanded by 11.36 mm at the angle of 85° and combines with the shear band of the specimen. Many different particle flakes and fragments are ejected out from shear fracture surface of the specimen.

Similarly, the ejector velocity of the left inclusion is 2.4235 m/s through the MATLAB software, the ejection velocity of the rock block cut-through by the left lower fracture and the tip of the inclusion is 3.3373 m/s, the ejection velocity of the upper right cement is 2.3857 m/s, the ejection velocity of the lower right cement is 2.1736 m/s, the ejection velocity of the right inclusion is 3.9044 m/s, and the ejection velocity of the rock broken at the right rear is 2.5137 m/s. Since the mass of the four blocks is

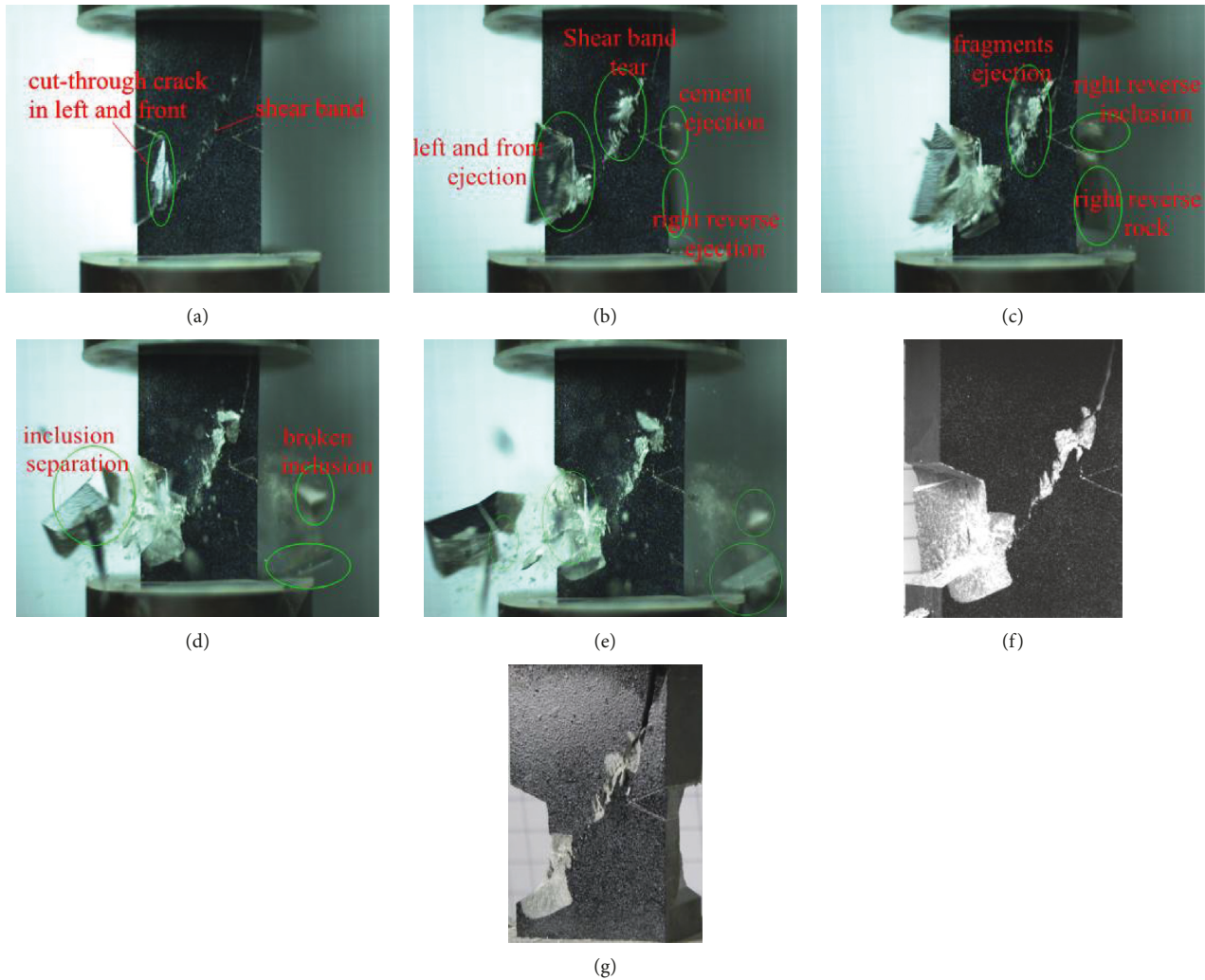


FIGURE 10: The ejection failure of specimen 4#. (a) 5.184000 s. (b) 5.181333 s. (c) 5.177333 s. (d) 5.165333 s. (e) 5.158667 s. (f) Failure (left). (g) Failure (right).

larger, the velocity in the horizontal direction is continuously reduced, and the vertical direction is gradually increased by the influence of gravity, which is shown in Figures 10(f) and 10(g) after failure.

3.3.5. Test of Specimen 5#. When the axial stress σ_z is 94.40 MPa in the loading of the specimen 5#, the curve shows a large drop fluctuation, which drops to 92.94 MPa, crack 1# with the upward cracking angle of 50° appears on the left lower prefabricated crack, and crack 2# with the lower cracking angle of 70° appears on the tip of the right inclusion. When the axial stress σ_z reaches 98.89 MPa in the continued loading, the curve appears to fall briefly, a small part of the tip of the left inclusion is broken, the upward cracks 3# and 4# appear from the broken point of the tip, and the angle between crack 3# and the vertical direction is 10° . When the peak stress σ_z is 116.137 MPa, crack 1# extends to the left inclusion, which is 5.45 mm from the left tip. At the same time, crack 4# with a cracking angle of 75° appears at the tip of the left inclusion and extends upward to the top of

the specimen. The secondary crack 2# from the tip of the right inclusion continues to extend to the bottom of the specimen, which is 6.36 mm from the lower right end of the specimen. The upward crack 5# with a cracking angle of 50° occurs at the end of the lower right prefabricated crack and grows to the surface of the test piece (Figure 11(a)). The shear-pull crack zone 6# appears in the middle of the specimen and combines with other cracks to cause severe failure, accompanying with severe noise. The left inclusion is completely extruded and ejected out, and the half tip of the right inclusion is ejected out in rockburst. A lot of white fragments in different sizes inside slip out, during the opening of the intermediate main shear crack, indicating that a large amount of energy is accumulated inside the specimen and used for rock failure (Figure 11).

Similarly, the ejection velocity of the left inclusion is 7.2873 m/s through the preliminary calculation of MATLAB software, the ejection velocity of the rock cut-through at the lower left crack and the tip of the inclusion is 7.0085 m/s, the ejection velocity of the upper crack of the left inclusion is 6.5037 m/s, the ejection velocity of the nearby internal rock

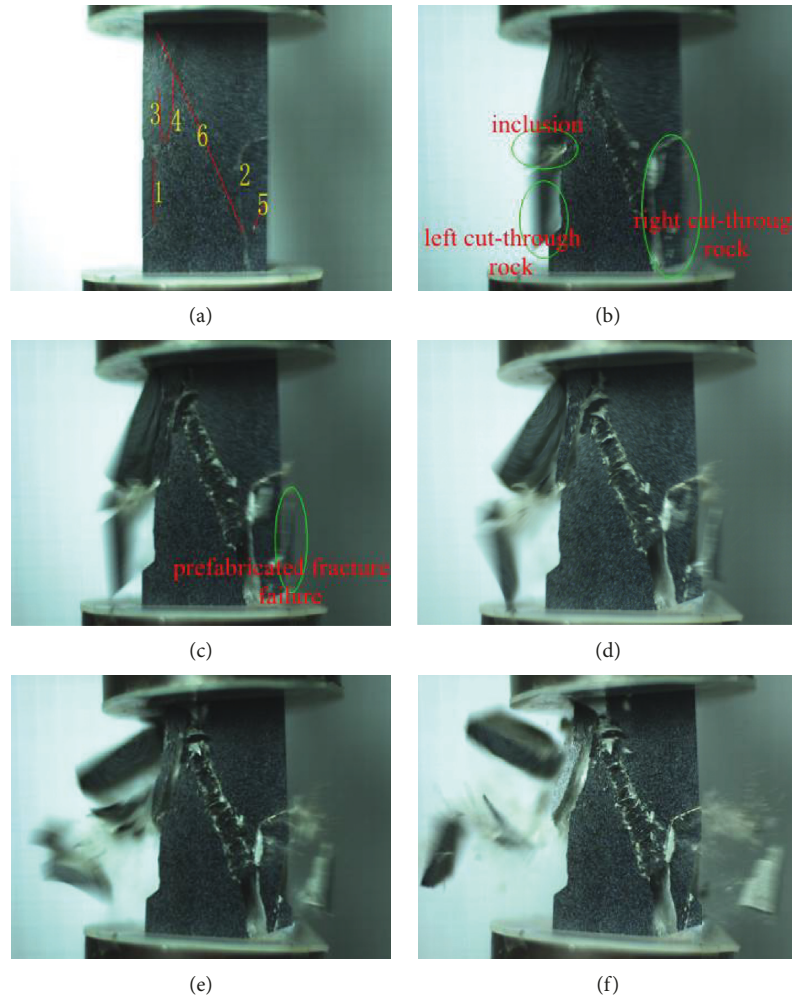


FIGURE 11: The ejection failure of specimen 5#. (a) 1.004000 s. (b) 1.002667 s. (c) 1.001333 s. (d) 1.000000 s. (e) 0.997333 s. (f) 0.993333 s.

mass is 3.2752 m/s, the ejection velocity of the fractured object on the right side is 6.4197 m/s, and the ejection velocity of the rock damaged at the lower right precut crack is 5.2484 m/s.

3.3.6. Test of Specimen 6#. When the axial stress σ_z is 90.97 MPa in the loading of the specimen 6#, the stress-strain curve drops to 89.32 MPa, and crack 1# appears at the end of the lower left preformed crack of the specimen and gradually expands upward at a crack angle of 50° . When the peak stress σ_z is 111.074 MPa, the curve shows a wave-fold increase, and the cement between the left and right inclusions and the rock is crushed and extruded, and crack 2# with an upwards cracking angle of 64° appears from the tip of the right inclusion. At the same time, the reverse crack 3# with the downward angle of 91° appears at the tip and combines with the lower right preformed crack. The crack 4# with a cracking angle of 80° upward appears at the tip of the left inclusion. The secondary crack 5# with a cracking angle of 40° appears at the end of the left prefabricated crack, extending to the tip of the left and left inclusions. The left and right inclusions are, respectively, ejected out, and the rock blocks formed after each crack penetration are also

ejected out. Due to the shear tensile stress, the shear cracks 2# and 3# are torn (Figure 12), and the damaged fragments in the cracks gradually collapse.

Similarly, the ejection velocity of the left inclusion of the specimen 6# is 7.4125 m/s, the velocity of the small rock near the left inclusion is 7.934 m/s, the ejection velocity of the rock block cut-through by the lower left crack and the tip of the inclusion is 5.3595 m/s, the ejection velocity of the right inclusion is 3.6242 m/s, the velocity of the rock block 1 at the lower right prefabricated crack is 5.8814 m/s, and the ejection velocity of the rock mass 2 is 6.6238 m/s.

3.4. Failure Analysis of Specimens. Figures 6~12 show the failure and ejection process of the specimens in the uniaxial compression test. The stress-strain curves, the shape of the fragments, and the fractures of the specimens are, respectively, shown in Figures 5 and 13.

Rock fragments in different sizes are produced in failure of inclusion rock model failure, which are accompanied by a large amount of energy consumption in the process of generating rock fragments. Since the lumpiness of rock fragments has statistical self-similarity, fractal dimension is an index to measure the characteristics of rockburst. The

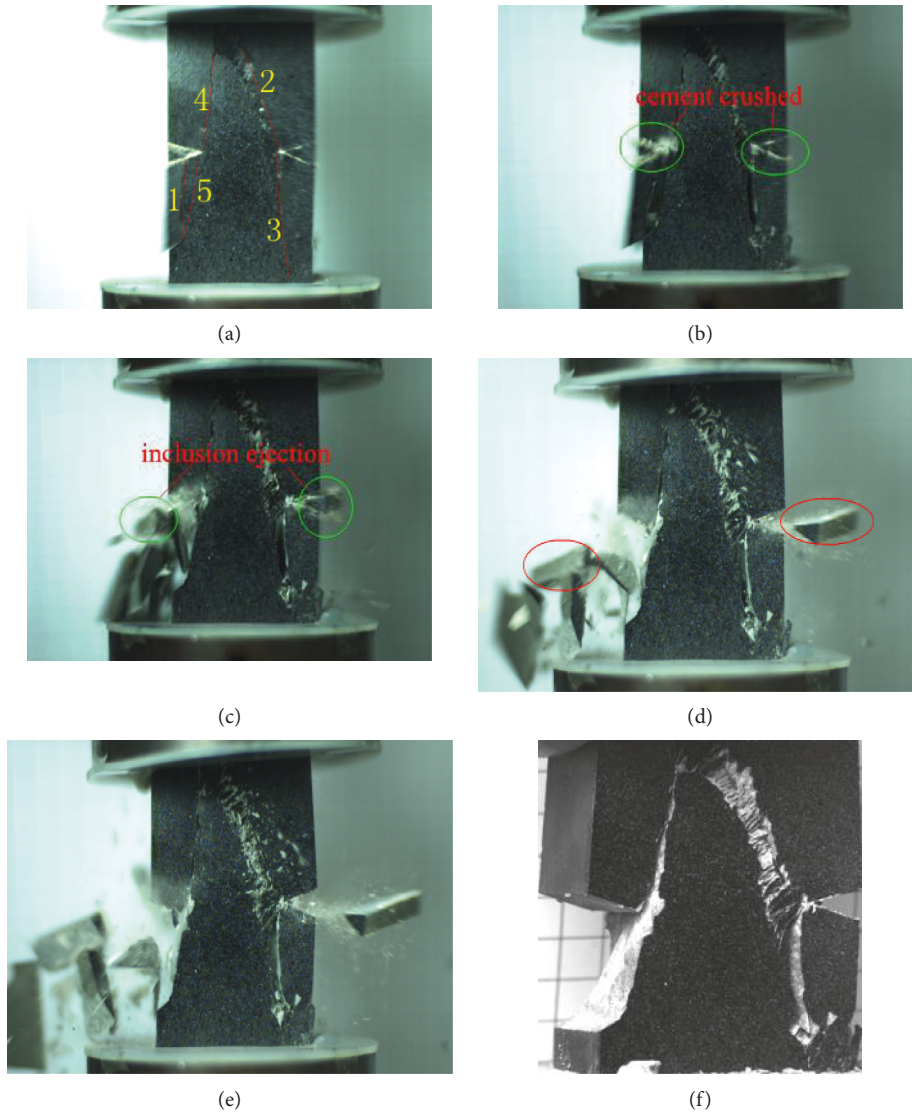


FIGURE 12: The ejection failure of specimen 6#. (a) 1.302667 s. (b) 1.301333 s. (c) 1.297333 s. (d) 1.290667 s. (e) 1.286667 s. (f) Final failure.

fractal dimension of rock lumpiness can well describe the degree of fragmentation and the amount of energy consumed in failure. Therefore, rock fragments in the size of larger than 3 mm are measured with a vernier caliper for the maximum size of the length, width, and thickness, and the mass of every rock fragment is weighed. The effective length of rock fragments of specimens is divided into sections based on the multiple (Table 2), and the fractal dimension is calculated by the mass M , the equivalent length L_{eq} of the fragment [25–27], which is given as follows:

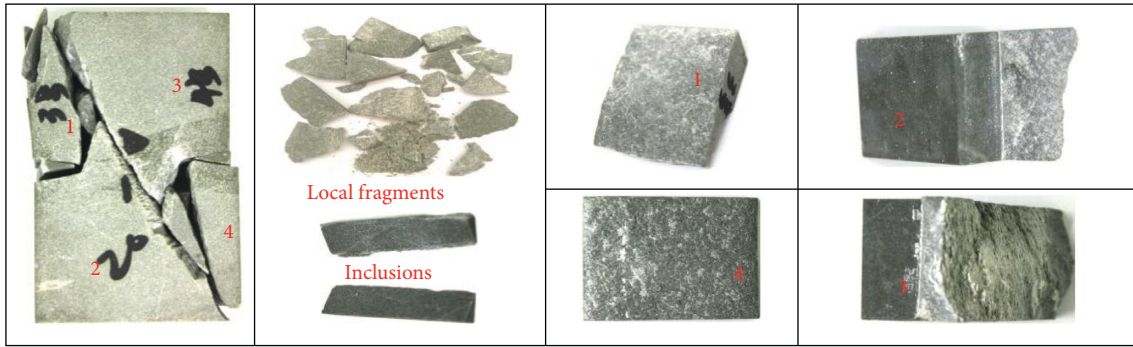
$$D = 3 - k, \tag{5}$$

$$k = \frac{\lg(M_{L_{eq}}/M)}{\lg L_{eq}},$$

where k is the slope of $M_{L_{eq}}/M - L_{eq}$ in double logarithmic coordinates, $M_{L_{eq}}/M$ is the cumulative percentage of rock fragments mass in the equivalent length $<L_{eq}$, $M_{L_{eq}}$ is the

mass of rock fragments in equivalent length L_{eq} , and M is the total mass of the rock fragments in the calculation scale. The equivalent side length L_{eq} is the side length converted into a cube by the length, width, and thickness of the rock measured. The relationship curve of $\lg M_{L_{eq}}/M - \lg L_{eq}$ is plotted, and the linear slopes of the six inclusions specimens are obtained by linear regression fitting, and the fractal dimensions $D = 3 - k$ are obtained. The calculation results are shown in Figure 14 and Table 3.

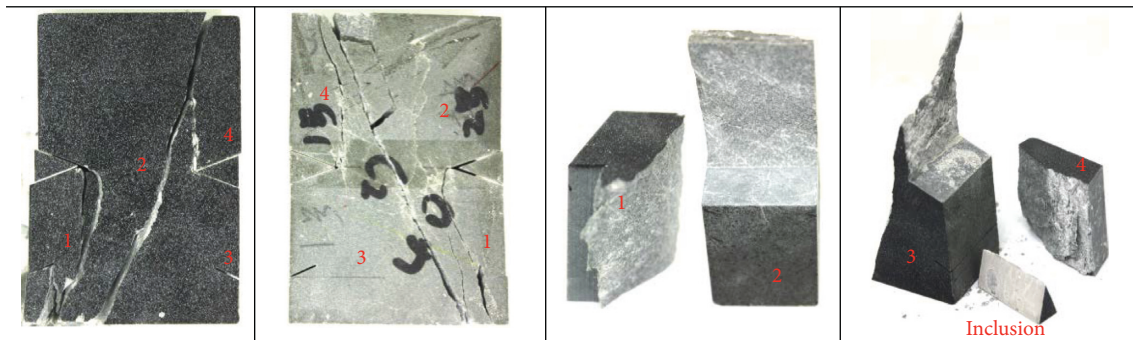
A large amount of energy is consumed in failure of the inclusion rock, which causes a large degree of failure, and the excess energy is provided to the ejection of rock fragments. The fractal dimension of rock fragments formed is related to the complexity of failure. Therefore, the fractal dimension can measure the complexity of the rock failure process; the larger the fractal dimension, the more the number of fragments, the higher the failure degree of the rock sample, and the more the energy consumption before the severe failure.



(a)



(b)



(c)



(d)

FIGURE 13: Continued.

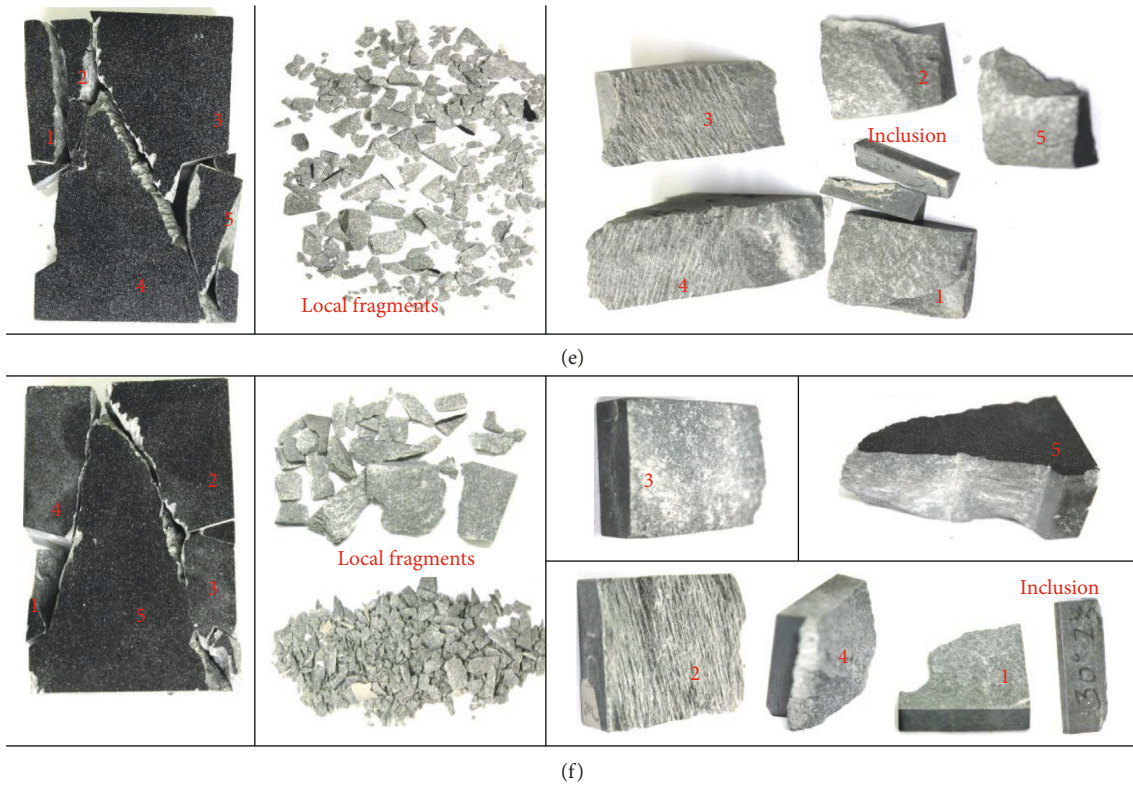


FIGURE 13: Failure characteristics of specimens. (a) Specimen 1#. (b) Specimen 2#. (c) Specimen 3#. (d) Specimen 4#. (e) Specimen 5#. (f) Specimen 6#.

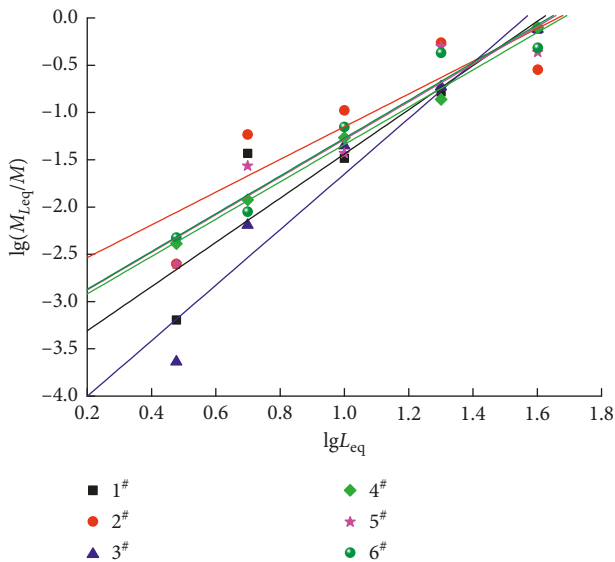


FIGURE 14: Fractal dimension calculated by granularity-mass relationships.

From the results of the above-mentioned inclusion rockburst model test, it can be seen that the pinch-off portion (tip) of the inclusions is severely damaged in uniaxial compression test, and cracks appear and expand continuously, causing the rock fragments formed by the cracks to eject out, accompanied by cracking sounds. Rock fragments in the surface and inside failure area of

the sample are broken and ejected out (white) in the process, and the entire sample is completely sheared and broken.

- (1) Based on the failure process and characteristics of specimens 1# and 2#, it can be found that the tip of the inclusion body is seriously damaged (turns white), and cracks appear on the basis of this and expand to the periphery, and the area cut-through is large. The peak stress, strain, and fractal dimension of specimen 2# with the cementation of inclusions and surrounding rock are larger than that of specimen 1# without cement, indicating the inclusions in the rock mass are cemented with the surrounding rock and the better the cementation, so the higher the strength, the larger the deformation before failure, the more the energy accumulated, the larger the energy consumption before the sudden failure, the more the formation of rock fragments, and the greater the degree of failure.
- (2) For specimens 3#, 4#, 5#, and 6# with symmetric preformed cracks and cementation, the failure strength and fractal dimension values of the specimens are lower than that of specimen 2#; the preformed cracks can reduce the failure strength of the inclusions and the generation of fragments.
- (3) The failure strength and fractal dimension of specimens 4#, 5#, and 6# with the cemented inclusions and preformed cracks are higher than that of specimen 1#

TABLE 3: Fractal dimension of fragments of rock.

Specimen number	The division equivalent side length/mm	Fit the linear equation	Coefficient of association R	Fractal dimension D
1#	>40	$y = 2.3379x - 3.7770$	0.8475	0.6621
2#	40~20	$y = 1.7309x - 2.8813$	0.8057	1.2691
3#	20~10	$y = 2.9385x - 4.58998$	0.9171	0.0615
4#	10~5	$y = 1.9740x - 3.3132$	0.9909	1.0260
5#	5~3	$y = 1.9904x - 3.2755$	0.8453	1.0096
6#		$y = 1.9976x - 3.2695$	0.9238	1.0024

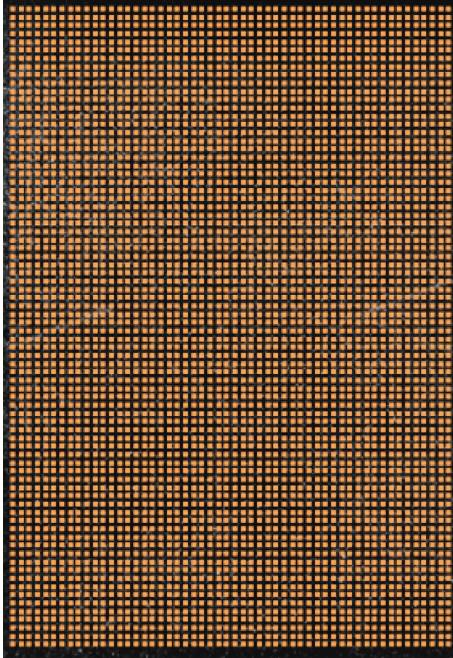


FIGURE 15: Digital marking points.

without the cementation and preformed cracks, indicating no cementation (reducing the cementation between inclusions and the surrounding rock) is more conducive to reducing the failure strength of the rock than by pressure relief of prefabrication cracks, and it is not easy to form more fragments, and the consumption of surface energy is also less.

- (4) The larger the tip angle of the inclusions, the greater the stress loading required in failure for specimens 3# and 6# and specimens 4# and 5# in the same length of prefabricated crack; in other words, the failure strength of specimen 3# is greater than that of specimen 6#. However, due to the heterogeneity of the rock, many large cracks appear before failure of specimen 3#, so that a large amount of energy is consumed here, and fewer large cracks appear and extend, that is, the fractal dimension of specimen 3# is much lower than that of specimen 6#. The failure strength and fractal dimension of specimen 4# are larger than that of specimen 5#; the reason is that the larger the tip angle of the inclusions, the larger the volume of the inclusions, the more inclined the force surface, the greater the support effect of the inclusions on the surrounding rock mass, and the greater the force required to be overcome in failure. Moreover, it

is easy to form more small cracks under high stress intensity to generate more small-sized fragments.

- (5) The larger the length of the preformed crack, the more prone the crack propagation to failure, and the smaller the peak stress in failure of the specimen, the smaller the number and scale of fragments for specimens 3# and 4# and specimens 5# and 6# in the same angle of inclusion tip.

In summary, in order to reduce the threat to surrounding people, equipment, and engineering in inclusion rockburst, it is possible to reduce the degree of cementation between the inclusions and the surrounding rock mass, increase the length of the prefabricated cracks, and increase the angle of the inclusions tip, which can reduce the failure degree of the rock mass.

4. Analysis of Digital Image Correlation Method

The digital image correlation method (DIC) [28] is a full-field, noncontact optical measurement method that directly extracts deformation information from randomly distributed spots or pseudorandom distribution artificial speckle fields. The basic principle is to match the geometric points on the digitized speckle image in different states of the surface of the object and track the movement of the point to obtain the deformation information of the surface of the object. Given $f(x, y)$ before image deformation and $g(x, y)$ after image deformation, the image subregion corresponding to the image before deformation is identified in the deformed image, and correlation matching operation is performed.

The MV-VD500SM/SC camera is used to record the image of every moment (the speckle movement) in the uniaxial compression process of the inclusion model specimen, and the shooting speed is 1 piece per second. The digital image processing program compiled by MATLAB is used to process the acquired image and convert it into a DIC image with a resolution of 700 pixels \times 1200 pixels. The digital marker points are set in the image, and the distance between the adjacent points is 20 pixel \times 20 pixel (Figure 15), and the displacement of every point is calculated in the speckle field; the graph is drawn based on the obtained data to measure the horizontal displacement field (u) and the vertical displacement field (v) in the compression process of the inclusion model specimen, and the displacement field before failure immediately is selected, which is shown in Figure 16.

Figure 16 shows the instantaneous u and v displacement fields (magnitude and direction of displacement in the surface of the specimen) of specimens 3#, 4#, 5#, and 6#

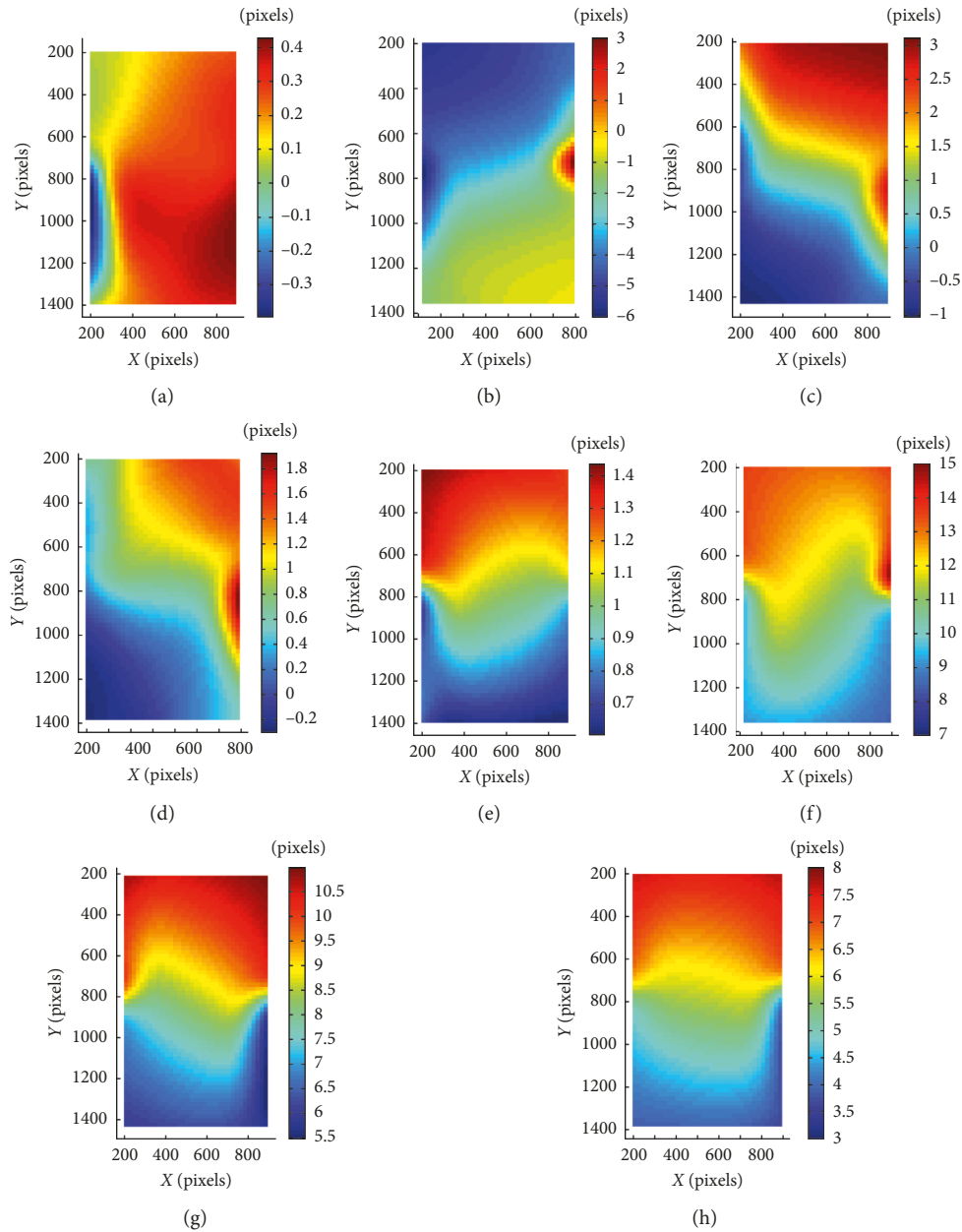


FIGURE 16: The displacement field of inclusion rock specimens before failure. (a) Specimen 3#(u). (b) Specimen 4#(u). (c) Specimen 5#(u). (d) Specimen 6#(u). (e) Specimen 3#(v). (f) Specimen 4#(v). (g) Specimen 5#(v). (h) Specimen 6#(v).

obtained by the digital image correlation method, which is consistent with the deformation and failure results of the specimen in the test. Cracks of specimens 4#, 5#, and 6# generate and expand during the deformation process in the uniaxial compression test, resulting in severe ejection failure. The specimen 3# only suffers from the static failure of the crack propagation without the ejection phenomenon; the reason is that a certain degree of heterogeneity exists in the rock material. Many secondary cracks appear and expand at the tip of the inclusion body and the preformed crack before failure of specimen 3#, which greatly dissipates the energy accumulated during the loading process, and the specimen breaks finally in the peak stress, so that the displacement fields in the horizontal (u) and vertical (v) of

specimen 3# are much smaller than those of the other three specimens in the event of major failure. In the displacement u of the specimen, the left and right inclusions and the rock mass between the preformed cracks are, respectively, moved and deformed in the direction of left and right, and the u displacement field has a negative value to the left and a positive value to the right. The displacement of the lower part of the left inclusion of specimen 3# is about 0.3 pixels in horizontal leftward, and the displacement of the area near the right inclusion is between 0.2 and 0.4 pixels in horizontal rightward.

The specimens 4#, 5#, and 6# exhibit an oblique symmetry change in the direction of u displacement, which corresponds to the crack penetration during the test. The left

inclusion and the lower cut-through part of specimen 4# cause the upper part of the area to have no support, so that the left and lower parts are displaced. It can be seen from Figures 10, 16(b), and 16(f) that the inclusion body and the leftward area of the specimen are 4 to 6 pixels in horizontal displacement (u), and the vertical displacement (v) is downward 12 to 14 pixels. There is no crack propagation failure in the front region of the right inclusion; only the cement in the right inclusion and the specimen is crushed and ejected out, so that the change of the displacement to the right is great in the right inclusion; the displacement field u is 1 to 3 pixels, and the displacement field v is 13 to 15 pixels.

It can be seen from Figures 11, 16(c), and 16(g) in specimen 5# that the local area of the specimen in the deformation and failure corresponds to the u and v displacements obtained by the digital image, that is, the specimen is subjected to tensile shear failure in the lower left and upper right. The horizontal displacement of the lower left rock mass of the specimen is 0 to 1 pixels, and the horizontal displacement of the lower right rock block is 1.5 to 3 pixels. The cut-through cracking failure occurs in the left inclusion and the upper and lower local regions, the corresponding displacement field (Figure 16(c)) is the tip and strip region in the lower left, and the displacement changing to the left is 0.5~1 pixels. Due to the blocking effect of the inclusions on the vertical displacement of the specimen, the v displacement field changes greatly in the vicinity of the inclusion, and the value is 6.5 to 10 pixels. The right inclusion and its lower region are cut-through, the u displacement field is 2 to 3 pixels, and the v displacement field is 6 to 8 pixels.

It can be seen from Figures 12, 16(d), and 16(h) in specimen 6# that the left and right inclusions and its upper and lower regions are cut-through cracking, and the change in the displacement field is relatively uniform. The horizontal change of displacement in the left failure region is 0 to 0.2 pixels, and the v field displacement is 4.5 to 7 pixels. The change of the u displacement field in the right failure region is 0.6 to 1.8 pixels, and the v field displacement is 3.5 to 7 pixels.

The change of the u and v displacements of specimen 5# is greater than that of specimen 6# in deformation and failure; the reason is that the length of preformed crack of specimen 5# is smaller than that of specimen 6#, and the shorter the length of the crack, the more difficult the rock to be destroyed, the higher the peak stress, and the greater the displacement change before failure. The change of the u and v displacements of specimen 4# is greater than that of specimen 5# in deformation and failure, which indicates that the larger the angle of the tip of the inclusion is, the greater the stress is, and the larger the displacement of the specimen surface is. It is consistent with the law of the stress-strain curve in the test.

The variation law of the four specimens in the direction of the v displacement field is consistent. A large change of displacement occurs above the horizontal band between the inclusions, and the changed displacement in vertical direction near the horizontal band of the inclusion and the area below is reduced; the stratification is obvious, indicating

that the inclusions suppress the change of the vertical displacement, the middle area in the vertical displacement field is elliptical, and the displacement of the middle region is larger than the change of the v displacement near the left and right inclusions in the vicinity of the horizontal band, which causes the inclusions to withstand a large concentration of stress and becomes prone to damage.

5. Analysis of Finite Element Simulation

The finite element software ANSYS 17.0 is used to simulate and analyze the six model specimens in inclusion rockburst test. Based on the size of inclusion specimens (Figure 3), the element type of mud shale rock and cement of models are both three-dimensional solid structural unit SOLID185 with 8 nodes, and every node includes three degrees of freedom to translate along the x - y - z direction. The mesh size of six models is 2 mm, and there is no cement between the inclusions and the surrounding rock in specimen 1#. The cement, the inclusions, and the specimens are bonded by the command of Glue in specimens 2# to 6#. Local fine division (level 3) is in tip of the model inclusions and the prefabricated cracks (Figure 17).

The material parameters are shown in Table 1. The displacement of the bottom surface of the model is constrained in u_y direction, and the four sides of the bottom of the model are subjected to the displacement constraint in u_{xyz} direction. The displacement constraint of the surface is applied to the top surface of the model in the linear elastic condition; the displacement is the instantaneous displacement loading of the specimen before failure (Table 2). The distributions of strain energy density, von Mises stress, and x - y shear stress obtained after the model calculation are shown in Figure 18.

It can be seen from Figure 18 that the distribution of the stress and strain energy density obtained at the loading under the elastic condition is roughly consistent with the failure characteristics of the specimen and the displacement change obtained by the digital image method. In the finite element analysis of the specimen, the stress concentration region in the distribution of x - y shear stress is obliquely symmetrically distributed at the tip of the left and right inclusions, that is, light blue (upper left tip and lower right tip), yellow (lower left tip and right tip). The stress concentration gradually weakens from the tip end of the inclusions to the top and bottom of the model, which is consistent with the crack propagation failure from the tip of the inclusion in the test. However, the rock in the test is a heterogeneous brittle material, and there are defects inside, which leads to nonuniformity failure in the process of stress concentration, defects or serious defects near the tip of the inclusions, and the crack appear firstly in failure, and the chronological order of failure is right tip down-left tip-tensile failure in specimen 1#; the chronological order of failure is right tip down-left tip up-left tip up-right tip in specimen 2#. Similarly, the stress concentration region of the x - y shear stress distribution in finite element simulation of specimens 3# to 6# is also symmetrically distributed at the tip of the left and right inclusions. Due to the prefabricated

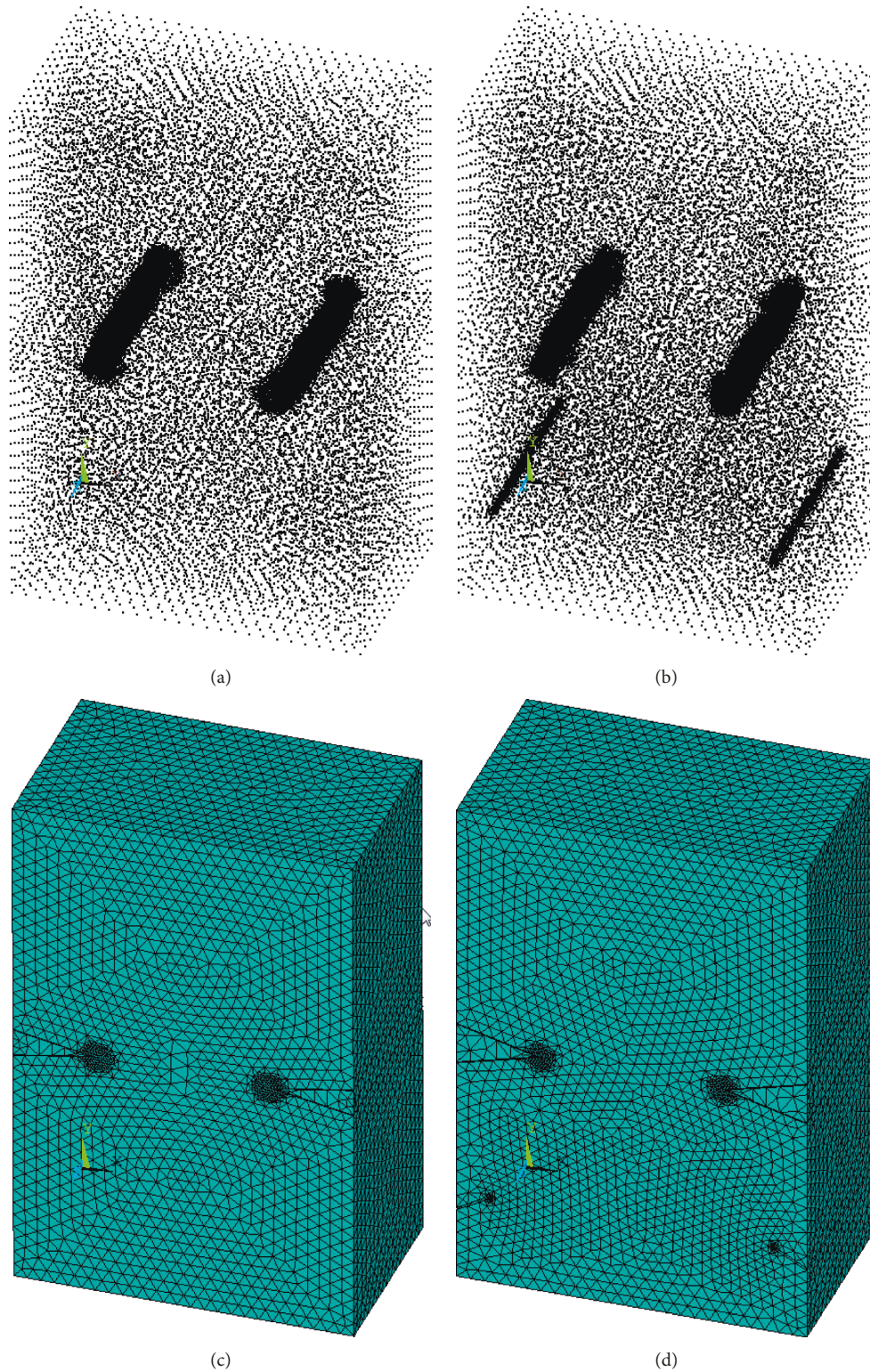


FIGURE 17: Nodes distribution and mesh generation. (a) Nodes distribution in no precast cracks. (b) Nodes distribution in precast cracks. (c) Mesh generation in no precast cracks. (d) Mesh generation in precast cracks.

cracks in the lower part of the specimen, the stress concentration appears near the tips of the cracks. In other words, a large stress concentration band appears between the tip of the inclusion body and the end of the fracture, which is

consistent with the fracture cut-through failure region in the lower portion of the tip in the test. The stress band in the tip of Inclusion body tip, the end of prefabricated crack, and the strip bottom area of specimens 3# to 6# is more concentrated

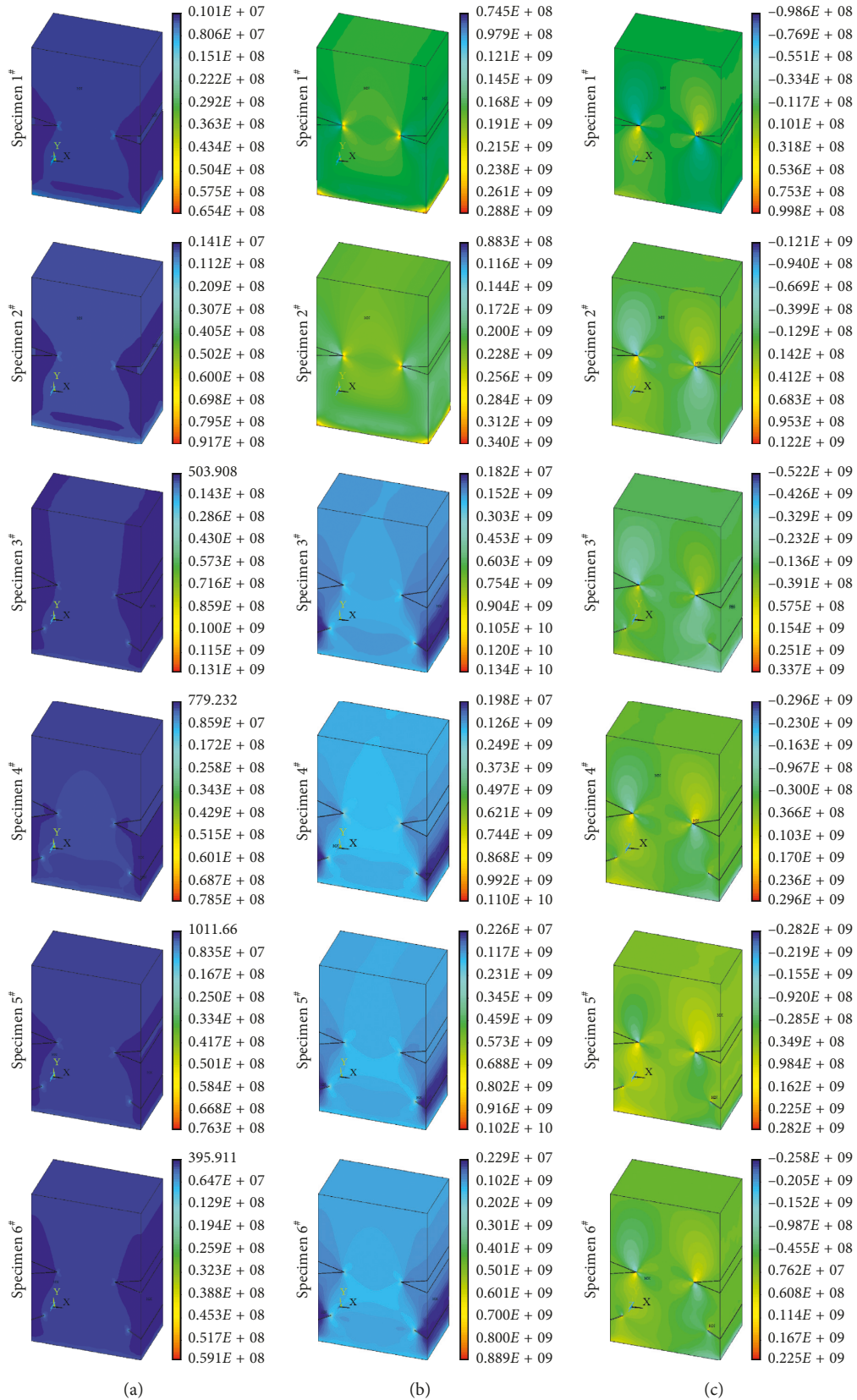


FIGURE 18: The distribution of strain energy density and stress. (a) Strain energy density. (b) von Mises stress. (c) x-y shear stress.

than those of specimens 1# to 2#, so the former is easy to break in this area. It can be seen that the results of finite element analysis agrees well with the experimental results in failure mode of the inclusion model specimens.

Figure 18(a) shows the energy density of every element of the six specimens before failure, and the strain energy accumulated during the load is calculated. Since the area under the stress-strain curve of the specimen is the work done by an external force on a rock mass unit [29, 30], the work (energy) of the specimen obtained by the test system before failure is calculated by the data obtained by the test, which is shown in Table 4.

It can be seen from the above table that the strain energy calculated in the finite element under elastic conditions is greater than the energy calculated in the test; the reason is that the rock in the test is a heterogeneous material, and there are natural defects, resulting in a decrease in energy accumulation. The energy difference affected by the length of the crack in the finite element calculation of specimen 3# and specimen 4# is 0.17 J, and the energy obtained in the test differs greatly. Cracks in the static failure of specimen 3# appear and extend continually during the loading before the peak stress, and the fracture consumed a part of the energy. It can be seen from Tables 2 and 4 that the energy change and the stress changes are consistent in specimens 3# and 6# and specimens 4# and 5#, that is, the larger the angle of the inclusions, the greater the failure stress, the larger the interaction between the inclusions and the rock, the more the stress concentration of the inclusions, and the more the energy accumulated; the distribution of the strain energy density is shown in Figure 18(a). The law of energy calculated is consistent with the results of experimental failure, fractal dimension calculated, and digital image method.

6. Conclusions

The classification of rockburst has always been one of the foundations for the study of rockburst problems. The model of inclusion rockburst is given in this paper. The simulation test on rockburst is carried out on specimens with inclusions by high-speed photography, digital image correlation method, and finite element simulation to study the failure mechanism of inclusion rockburst, and the effect of the angle of the tip of the inclusion and the preformed crack on the degree of rockburst is analyzed. The following conclusions are drawn:

- (1) The cracks appear from the tip of the inclusion and expand to the up and down direction in inclusion rockburst. The cracks expand in different orders of the left tip, the lower tip, the left tip, and the right tip; the cut-through rock mass would have been sharply ejected out when the accumulated energy is more, and the fractal dimension is larger. The static failure occurs in the low energy accumulated, and the fractal dimension is low. The lumpiness of rockburst fragments is lower in static load failure.
- (2) The analysis from the inclusions shows that the greater the compressive strength of the rock mass, the higher the energy accumulated, and the

TABLE 4: Energy calculation results before failure.

Specimen number	Energy calculated in test (J)	Energy calculated in ANSYS (J)
1#	115.0024	248.0150
2#	169.1664	342.2240
3#	74.2982	132.9330
4#	81.4208	132.7630
5#	75.4684	97.1995
6#	62.4404	68.8934

rockburst ejection damage is severe in the existence of cementation. Therefore, the degree of cementation between different rocks should be reduced in the prevention and control of inclusion rockburst.

- (3) The angle of the tip of the inclusion has a significant effect on the failure of the rock mass. The larger the angle of the inclusions is, the greater the strength is, the more difficult the failure is, and the larger the fractal dimension of the fragments formed after failure is. When the angle of inclusion is small, the displacement in horizontal and vertical is small. The inclusions have a barrier effect on the change of the rock sample in the vertical direction. The larger the angle of the inclusion is, the greater the barrier effect in the vertical direction is, and the more likely the stress concentration is, thus causing a large accumulation of energy.
- (4) Prefabrication crack near the inclusions helps to reduce the strength of failure and the accumulation of energy. The larger the length of the prefabricated crack is, the smaller the stress loading required in failure is, the smaller the energy accumulated is, and the smaller the fractal dimension of the fragment is, which can reduce the degree of rockburst.
- (5) From specimens 3# and 4#, the increase of the number of cracks and the extended length before failure of rock mass can contribute to the transformation of the dynamic failure of rock mass to the static failure, thereby reducing the occurrence of rockburst.

Data Availability

The data used to support the findings of this study are available from the corresponding author upon request.

Conflicts of Interest

The authors declare that there are no conflicts of interest regarding the publication of this paper.

Acknowledgments

This research was supported by the National Basic Research Program of China (973 Program) (2010CB226802 and

2011CB201201) and Natural Science Foundation of China (no. 41072242). We sincerely thank the staff at the Institute of Geology and Geophysics, Chinese Academy of Sciences.

References

- [1] X.-T. Feng and H. An, "Hybrid intelligent method optimization of a soft rock replacement scheme for a large cavern excavated in alternate hard and soft rock strata," *International Journal of Rock Mechanics and Mining Sciences*, vol. 41, no. 4, pp. 655–667, 2004.
- [2] Q. Qi, S. Chen, H. Wang et al., "Study on the relations among coal bump, rock burst and mining tremor with numerical simulation," *Chinese Journal of Rock Mechanics and Engineering*, vol. 22, no. 11, pp. 1852–1858, 2003.
- [3] Y. Jiang, H. Wang, S. Xue, Y. Zhao, J. Zhu, and X. Pang, "Assessment and mitigation of coal bump risk during extraction of an island long wall panel," *International Journal of Coal Geology*, vol. 95, no. 2, pp. 20–33, 2012.
- [4] Q. Qian and X. Zhou, "Failure behaviors and rock deformation during excavation of underground cavern group for Jinping I hydropower station," *Rock Mechanics and Rock Engineering*, vol. 51, no. 8, pp. 2639–2651, 2018.
- [5] M. He, L. R. Sousa, T. Miranda, and G. Zhu, "Rockburst laboratory tests database—application of data mining techniques," *Engineering Geology*, vol. 185, pp. 116–130, 2015.
- [6] Y. Jiang and Y. Zhao, "State of the art: investigation on mechanism, forecast and control of coal bumps in China," *Chinese Journal of Rock Mechanics and Engineering*, vol. 34, no. 11, pp. 2188–2204, 2015.
- [7] L. Xu and L. Wang, "Study on the rockburst type classification," *Journal of Geological Hazards and Environment Preservation*, vol. 3, no. 11, pp. 245–262, 2000.
- [8] H. Xie, L. Li, Y. Ju, R. Peng, and Y. Yang, "Energy analysis for damage and catastrophic failure of rocks," *Science China Technological Sciences*, vol. 54, no. 1, pp. 199–209, 2011.
- [9] X. Li, C. Li, W. Cao, and M. Tao, "Dynamic stress concentration and energy evolution of deep-buried tunnels under blasting loads," *International Journal of Rock Mechanics and Mining Sciences*, vol. 104, pp. 131–146, 2018.
- [10] H. Zhou, R. Xu, J. Lu et al., "Study on mechanisms and physical simulation experiment of slab buckling rockburst in deep tunnel," *Chinese Journal of Rock Mechanics and Engineering*, vol. 34, no. 2, pp. 3658–3666, 2015.
- [11] A. V. Dyskin and L. N. Germanovich, "Model of rockburst caused by cracks growing near free surface," in *Rockbursts and Seismicity in Mines*, A. A. Balkema, Ed., pp. 169–175, Taylor & Francis, Didcot, UK, 1993.
- [12] T. Li, C. Ma, M. Zhu, L. Meng, and G. Chen, "Geomechanical types and mechanical analyses of rockbursts," *Engineering Geology*, vol. 222, pp. 72–83, 2017.
- [13] F. Gong, Y. Luo, S. Xuefeng et al., "Experimental modeling on rockburst in deep hard rock circular tunnels," *Chinese Journal of Rock Mechanics and Engineering*, vol. 36, no. 7, pp. 1634–1848, 2017.
- [14] G. Su, Y. Shi, X. Feng, J. Jiang, J. Zhang, and Q. Jiang, "True-triaxial experimental study of the evolutionary features of the acoustic emissions and sounds of rockburst processes," *Rock Mechanics and Rock Engineering*, vol. 51, no. 2, pp. 375–389, 2017.
- [15] Y. Zuo, X. Li, Y. Zhang et al., "Calculation of ejection velocity of rock in rockburst caused by static-dynamic coupling loading," *Journal of Central South University: Science and Technology*, vol. 37, no. 4, pp. 815–819, 2006.
- [16] J. Zuo, C. Yan, Y. Sun et al., "Investigation on whole failure nonlinear model for deep coal-rock combined bodies," *Journal of Mining Science and Technology*, vol. 2, no. 1, pp. 17–24, 2017.
- [17] X. Sun, Q. Han, M. Chengyu et al., "Modeling test of deep buried tunnel in soft and broken rock based on non-contact monitoring methods," *Journal of Mining Science and Technology*, vol. 2, no. 3, pp. 235–242, 2017.
- [18] L. Ma and Q. Yang, "Study on effective properties of elastic media containing fluid inclusions," *Journal of Beijing University of Technology*, vol. 37, no. 8, pp. 1136–1142, 2011.
- [19] L. Chen, Z. Wang, and X. Cai, "Frost heave simulation of concrete canals based on inclusion constitutive theory," *Subgrade Engineering*, vol. 18, no. 5, pp. 7–10, 2011.
- [20] A. Kidybiński, "Bursting liability indices of coal," *International Journal of Rock Mechanics and Mining Sciences*, vol. 18, no. 6, pp. 295–304, 1981.
- [21] F. Gong, J. Yan, and X. Li, "A new criterion of rock burst proneness based on the linear energy storage law and the residual elastic energy index," *Chinese Journal of Rock Mechanics and Engineering*, vol. 37, no. 9, pp. 1993–2014, 2018.
- [22] S. Li, X. Feng, Y. Wang et al., "Evaluation of rock burst proneness in a deep hard rock mine," *Journal of Northeastern University (Natural Science)*, vol. 22, no. 1, pp. 60–63, 2001.
- [23] J. Guo, W. Wang, Z. Yang et al., "Research of coal pillar inducing rock burst in L-shaped zone working face and prevention technology," *Journal of Mining Science and Technology*, vol. 2, no. 1, pp. 49–57, 2017.
- [24] Q. Zhu, K. Xu, C. Zhang et al., "Study of performance monitoring of modified OPC mortar with CSA cement using piezoelectric sensors," *Engineering Journal of Wuhan University*, vol. 51, no. 5, pp. 418–421, 2018.
- [25] M. He, G. Yang, J. Miao et al., "Classification and research methods of rockburst experimental fragments," *Chinese Journal of Rock Mechanics and Engineering*, vol. 28, no. 8, pp. 1521–1529, 2009.
- [26] D. Liu, X. Zhang, M. He et al., "Study on sandstone fragments from impact rockburst experiments," *Journal of Mining Science and Technology*, vol. 3, no. 3, pp. 246–252, 2018.
- [27] C. Wang, H. Zhou, H. Pei et al., "Study on energy concentration and dissipation of Beishan granite in Gansu during failure process," *Journal of Mining Science and Technology*, vol. 3, no. 6, pp. 536–542, 2018.
- [28] Y. Zhao, Y. Xing, J. Huang et al., "Study on the fiber-reinforced concrete pull-out test using digital image correlation method," *Engineering Mechanics*, vol. 27, no. 6, pp. 169–175, 2010.
- [29] L. Li, H. Xie, J. Yang et al., "Experimental investigations of releasable energy and dissipative energy within rock," *Engineering Mechanics*, vol. 28, no. 3, pp. 35–40, 2011.
- [30] L. Li, Z. Xu, H. Xie et al., "Failure experimental study on energy laws of rock under differential dynamic impact velocities," *Journal of China Coal Society*, vol. 36, no. 12, pp. 2007–2011, 2011.



Hindawi

Submit your manuscripts at
www.hindawi.com

